

## Electron Transfer-Induced Blinking in Ag Nanodot Fluorescence

Sandeep A. Patel,<sup>†</sup> Matteo Cozzuol,<sup>†,‡</sup> Joel M. Hales,<sup>†,‡</sup> Chris I. Richards,<sup>†</sup> Matthew Sartin,<sup>†,‡</sup> Jung-Cheng Hsiang,<sup>†</sup> Tom Vosch,<sup>†</sup> Joseph W. Perry,<sup>†,‡</sup> and Robert M. Dickson<sup>†,§,\*</sup>

*School of Chemistry and Biochemistry and Petit Institute of Bioengineering and Bioscience, Center for Organic Photonics and Electronics, Georgia Institute of Technology, Atlanta, Georgia 30332-0400*

*Received: August 17, 2009; Revised Manuscript Received: October 7, 2009*

Various single-stranded DNA-encapsulated Ag nanoclusters (nanodots) exhibit strong, discrete fluorescence with solvent polarity-dependent absorption and emission throughout the visible and near-IR. All species examined, regardless of their excitation and emission energies, show similar microsecond single-molecule blinking dynamics and near IR transient absorptions. The polarity dependence, microsecond blinking, and indistinguishable microsecond-decaying transient absorption spectra among multiple nanodots suggest a common charge transfer-based mechanism that gives rise to nanodot fluorescence intermittency. Photoinduced charge transfer that is common to all nanodot emitters is proposed to occur from the Ag cluster into the nearby DNA bases to yield a long-lived charge-separated trap state that results in blinking on the single molecule level.

### I. Introduction

Fluorescence intermittency (“blinking”) is a significant limitation to attaining high, sustained emission rates from single molecules and to tracking long-time single molecule dynamics. Although isomerization,<sup>1</sup> intersystem crossing,<sup>2</sup> and Auger-based<sup>3</sup> (photoinduced charge transfer) blinking mechanisms have been proposed, direct observations of the states causing intermittency are rare due to challenges in synchronization of stochastic individual molecule trajectories on the microsecond to second time scales. Recently, we developed a new class of fluorophores consisting of few-atom silver clusters encapsulated in single-stranded DNA (ssDNA). While the highly polarizable electrons of bulk silver result in many advantageous electronic and optical properties,<sup>4,5</sup> clusters consisting of only a few atoms exhibit discrete electronic transitions, properties more akin to molecular behavior. For example, water-soluble, fluorescent, oligonucleotide-encapsulated silver clusters (Ag nanodots) show bright, photostable emission throughout the visible and near-IR regions.<sup>6,7</sup> As long as the highly polarizable Ag cluster electronic states are discrete and continuous band energies are not exhibited, fluorescence can be a major relaxation pathway for the cluster excitation.<sup>8–10</sup> Unprotected Ag clusters of similar size, however, also exhibit significant (>10%) electron photoejection that nonradiatively dissipates absorbed energy,<sup>11,12</sup> due to the strong absorption and low ionization potentials of highly polarizable metal electrons within molecular scale clusters. As clusters grow beyond 1 nm in diameter, fluorescence and electron photoejection both become inefficient decay pathways relative to plasmonic reradiation (scattering) and nonradiative dissipation.<sup>11,12</sup> The strong fluorescence of ssDNA-encapsulated nanodots, which is complementary to both organic dyes and much larger semiconductor quantum dots, are being actively investigated for use in biological imaging.<sup>13,14</sup>

Fluorophores typically exhibit blinking at the single molecule level due to the presence of dark states formed following photoexcitation. Because of their relatively long lifetimes, these dark states facilitate saturation of absorption, thereby limiting both sensitivity and the ability to continuously track dynamics of individual molecules. Although silver nanodots<sup>7,15,16</sup> typically exhibit faster dark-state decay relative to organics<sup>17</sup> and quantum dots,<sup>18</sup> transitions to such dark states still place limitations on the sustainable emission rates of single nanodots.<sup>16</sup> These dark states, however, can be advantageously employed as photo-switches for improvements in both spatial resolution<sup>17,19</sup> and detection sensitivity,<sup>20,21</sup> although only isomerization-based photoswitches exhibiting thermally stable dark states have thus far been reported. In contrast, Ag nanodots exhibit photoaccessible dark-states with  $\sim 10 \mu\text{s}$  characteristic decay times,<sup>16</sup> that can be optically depopulated faster than their natural decay time.<sup>15</sup> Such direct dark state excitation enables optical modulation of fluorescence and highly sensitive signal recovery through photoinduced dark state relaxation (termed SAFIRE, or synchronously amplified fluorescence image recovery).<sup>15</sup> This not only significantly increases emission rates through optically induced dark state depopulation but can greatly improve sensitivity through detection of modulated signals, thereby taking advantage of the blinking process.<sup>15</sup> Consequently, it is of great interest to understand and exploit the optically addressable, metastable dark states that enable efficient optical modulation of Ag nanodot fluorescence.

As silver salts are only weakly soluble in the absence of a ligand, and bare gas-phase clusters efficiently photodissociate at visible energies,<sup>9,22,23</sup> a DNA scaffold that binds and encapsulates is crucial to Ag nanocluster stability and fluorescence.<sup>6</sup> In contrast to the characteristic atom or dimer loss resulting from visible excitation of gas phase Ag clusters,<sup>23</sup> unprotected aqueous Ag nanoclusters exhibit  $\sim 10\%$  quantum yields of electron photoejection,<sup>24,12,25</sup> leading to dissipation of absorbed energy that often exceeds the dissociation threshold of the ground state of the cluster.<sup>9</sup> Interestingly, nucleotide bases can be efficient electron acceptors,<sup>26–28</sup> suggesting that excited-state charge transfer from Ag clusters to DNA bases may play

\* To whom correspondence should be addressed. E-mail: robert.dickson@chemistry.gatech.edu.

<sup>†</sup> School of Chemistry and Biochemistry.

<sup>‡</sup> Center for Organic Photonics and Electronics.

<sup>§</sup> Petit Institute of Bioengineering and Bioscience.

a role in the observed blinking dynamics. Furthermore, the dual laser fluorescence modulation<sup>15</sup> of the oligonucleotide-encapsulated Ag nanodots appears to result from an interaction between the highly polarizable silver cluster excited-state and the oligonucleotide.

Here, we link the single-molecule blinking dynamics of several oligonucleotide-encapsulated silver nanodots<sup>7</sup> with bulk dark-state transient absorption measurements on aqueous nanodot solutions. These complementary investigations of the photoaccessed dark state reveal very similar photophysics, suggesting that the same states are being probed in the two very different measurements. Additionally, femtosecond transient absorption measurements of the excited-state dynamics provide information necessary to generate a state model for early time dynamics. Together, the time-resolved studies support a model involving subpicosecond photoinduced charge transfer, that leads to a small dark state population (~1% yield) that persists out to ~10  $\mu$ s. This dark state is likely to be that which yields single nanodot blinking and dual laser fluorescence enhancement.<sup>15</sup> Thus, in this picture, the dark state decay times can be reduced with high-intensity cw laser excitation<sup>16</sup> through optically induced repopulation of the fluorescent state. Accordingly, the overall emission rates can be tuned by controlling the relative excitation rates of the two states, achieved either by adjusting the intensity of the ground-state excitation laser or by introducing a second, red-shifted laser for direct dark state excitation.<sup>15</sup>

## II. Experimental Methods

The synthesis of red and near-IR absorbing Ag nanodots has been described previously.<sup>7</sup> Femtosecond transient absorption spectra were acquired using a commercially available pump–probe spectroscopy system (Newport, Helios). The pump wavelength was tunable from 465–2900 nm and the pulses (~120 fs, fwhm) were generated from an optical parametric amplifier (Newport, TOPAS), which in turn was pumped by a Ti:Sapphire regenerative amplifier (Newport, Spitfire) operating at a repetition rate of 1 kHz. The probe pulse was obtained by using approximately 5% of the amplified 800 nm output from the Spitfire to generate a white-light continuum (420–800 nm) in a sapphire plate. The temporal step resolution of the system was 7 fs and the maximum extent of the temporal delay was 3200 ps. The instrument response function was determined to be ~150 fs. At each temporal delay, data were averaged for 1.5 s. The pump beam was chopped at 500 Hz to sequentially obtain pumped (signal) and nonpumped (reference) absorption spectra of the sample. A correction factor to account for the chirp of the white-light continuum probe was generated using the ultrafast response of CHCl<sub>3</sub> and was applied to all data sets. The data were stored as three-dimensional (3D) wavelength-time-absorbance matrices that were exported for use with the fitting software. The solutions were studied in 2 mm path-length cuvettes and were stirred continuously throughout the data acquisition.

Nanosecond transient absorption measurements were performed as pump–probe experiments. A white light source (Newport, 250 W tungsten lamp, 300 W radiometric power supply model 69931) served as the probe while the pump is a tunable nanosecond laser (Newport- Spectra-Physics, PRO-250-10, 8 ns pulse, pumping an OPO: Newport- Spectra-Physics, MOPO-PO). The energy is varied by using two beam splitter cubes, each one preceded by a half wave plate. The waveplate orientation is controlled by a rotary stage (Newport, PR50-PP) and a motion controller (Newport, ESP-300). To work with a flat top beam and easily calculate the fluence, the laser beam is

expanded (4 $\times$ ) by a telescope, and the central part is selected by using a 1 cm iris. Pulse energy is measured with a pyroelectric detector connected to a power meter (OPHIR, PE25BB, and NOVA II) and is constantly monitored during the measurement by a fast, amplified silicon PIN detector (Newport, 818-BB-21A). The angle between the pump and probe light is kept as small as possible (<~2°). Single wavelength transient absorption temporal response was recorded using a monochromator (Acton, SP150) and a Si PIN photoreceiver (Femto, HCA-S-200M-SI) for the visible and a InGaAs PIN photoreceiver (Femto, HCA-S-200M-IN) for the near-IR part of the spectrum. Transient signals from the photoreceiver are synchronously triggered with the pump pulse, captured using a 300 MHz digital oscilloscope (Tektronix, TDS 3034b), and transferred to a PC via a GPIB interface. Gated transient spectra between 300–900 nm were taken using a spectrometer (Acton, 320PI) and a CCD camera (Princeton Instruments, ST-133). A delay generator (Berkeley Nucleonics, model 575) was used to control the initial delay between the pump pulse and the start of the data acquisition. The hardware controlling the camera allows for tuning of the gate width, delay time, and signal gain. Dedicated Labview software is used to generate wavelength versus time 2D arrays of  $\Delta$ OD values for each single measurement.

Fluorescence correlation spectroscopy (FCS) time traces were taken by exciting with a continuous-wave HeNe laser (594 nm or 633 nm, Melles Griot) focused into a diluted sample solution by a 60 $\times$ , 1.2 NA water immersion objective (Olympus UPlan Apo). Emission was collected by the same objective and focused onto an avalanche photodiode (Perkin-Elmer), and the time traces were generated by a time-correlated single photon counting board (Picoquant, Timeharp).

## III. Results

Various Ag nanodots with absorption and emission ranging from blue to near-IR wavelengths have been created by specifically tailoring the encapsulating DNA nucleotide sequence. In this paper, the photophysical dynamics giving rise to blinking for three red to near-IR emitting species, Ag660, Ag680, and Ag710, are elucidated. These species exhibit excited-state emissive lifetimes ranging from 3 to 3.5 ns and fluorescence quantum yields ranging from 17 to 34%, but the hydrodynamic radii ( $R_H$ ) of all emitters are indistinguishable, as the ~2.5 nm  $R_H$  results primarily from the 12-mer ssDNA scaffold.<sup>29</sup> Previous single-nanodot studies revealed a single blinking time scale, corresponding to 5–40 microsecond off-times, which limits the overall emission rates.<sup>16</sup> Higher intensity excitation reveals a sublinear relationship between excitation and emission intensities, but no clear saturation, as both on- and off-times gleaned from single-nanodot emission decrease with increasing incident intensity.<sup>16</sup> Further, significant solvatochromism is observed suggesting a large change in dipole moment between ground and emissive excited states. In Figure 1, a Lippert–Mataga plot of the Ag660 is shown, plotting the Stokes shift as a function of the solvent reaction field, according to the following equation<sup>30</sup>

$$\nu_1 - \nu_0 = \frac{2(\mu_1 - \mu_0)^2}{hca^3} \left( \frac{\epsilon - 1}{2\epsilon + 1} - \frac{n^2 - 1}{2n^2 + 1} \right) \quad (1)$$

in which  $\nu_1$  and  $\nu_0$  are the frequencies of the absorption and emission maxima,  $a$  is the Onsager radius,  $\mu_1$  and  $\mu_0$  are the dipole moments of the emissive and ground states, respectively,

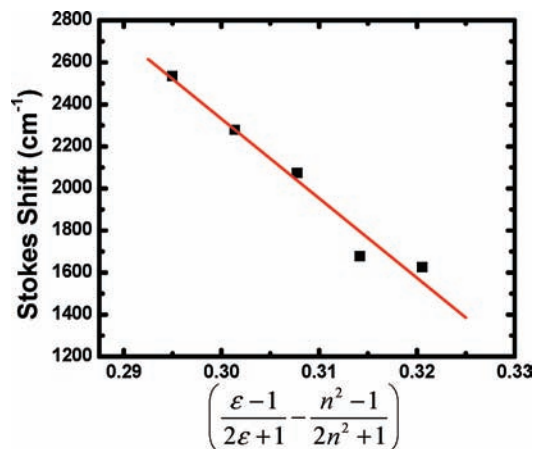


**Figure 1.** Lippert–Mataga plot of the 660 nm emitting species. The solvent dielectric function was changed by the variation of the ethanol–water ratio. The absorption and emission spectra were measured in each solvent and the slope of the fitted line was used to calculate the dipole change from the ground state to the excited state, according to the Lippert–Mataga equation. The change was calculated to be  $16.0 \pm 1.1$  D.

$\epsilon$  is the static dielectric constant of the solvent, and  $n$  is the solvent refractive index. The slope of the linear fit was then used to calculate the dipole moment change ( $\mu_1 - \mu_0$ ) which for the Ag660 emitter was found to be  $16.0 \pm 1.1$  D, assuming an Onsager radius of 0.4 nm, estimated from the expected radius of a  $\sim 10$  atom Ag cluster bound to cytosine. The large change in dipole and the negative slope suggest that significant charge separation occurs upon excitation and less so upon emission, indicating that there is a reduction in charge separation on relaxation to the emissive state.

Transient absorptions at short time scales (femtoseconds to nanoseconds, Figure 2), with  $\sim 100$  fs excitation, reveal rapid ( $\sim 350$  fs) population of an excited state absorption that is both broader and red-shifted relative to the nanodot ground-state, low-energy absorption band (e.g., 595 nm for the Ag660 nanodot). These fast transient absorption spectra resemble the spectrum of the dual-laser-induced fluorescence enhancement recently reported, through optically induced dark state decay.<sup>15</sup> Although the general features of the different nanodot transient spectra are similar, a noticeable blue shift of the peak of the transient absorption between the “early” time ( $< 3$  ns) spectra and spectra taken at 60 ns (Figure 3) is evident. Coupled with the polarity effects on Stokes shift (Figure 1), the blue shift suggests that this is associated with a distinct state or geometry formed by relaxation from the initially excited charge transfer state. To obtain the “actual” transient absorption spectra and the amplitudes of the time transients at different wavelengths, it was necessary to correct for overlap between the ground state bleaching and induced transient absorptions. The kinetic traces of the ground-state recovery (Figure 2) were corrected for contributions from the transient absorption at wavelengths sufficiently far from the ground state absorption. This was justified based on identical kinetics being observed on both sides of the transient spectrum (at  $\sim 520$  and 775 nm) and enabled separation of the transient absorption temporal components. The result is an increased  $\Delta OD$  depletion at 579 nm, which is then largely dominated by the ground-state recovery kinetics. Similar corrections were made for all emitters. The ground state recovery kinetics reveal multiple pathways of ground-state repopulation, as indicated by the various time scales. The Ag660 ground-state bleach, for example, recovers with time constants of  $\sim 500$  fs ( $k_{10} = 2 \times 10^{12} \text{ s}^{-1}$ ) and  $\sim 2$  ns ( $k_{20} = 5 \times 10^8 \text{ s}^{-1}$ ), each

resulting from decay of a different excited-state following excitation. Since nonradiative decay occurs at approximately  $2 \times 10^{12} \text{ s}^{-1}$ , direct competition between these radiative and nonradiative relaxation processes cannot be occurring as otherwise no emission on the 2 ns time scale would be observable. It should be noted that the 2 ns decay time is consistent with the measured fluorescence lifetime, supporting the assignment to an emissive state. The 350 fs rise time of the transient absorption (Table 1) indicates that formation of the emissive state (state 2) takes place with  $k_{12} = 2.9 \times 10^{12} \text{ s}^{-1}$ , likely before significant vibrational relaxation can occur, which decays with the same 2 ns time constant as observed in the bleach recovery. It is therefore proposed that an initially formed charge separated state (state 1) undergoes branching nonradiative relaxations to the ground state ( $\sim 500$  fs recovery time to state 0) and to a fluorescent excited state (state 2, which is formed with a  $\sim 350$  fs rise time) that has a  $\sim 2$  ns emissive lifetime. This level scheme is diagrammed in Figure 4. The relative time constants of 350 and 500 fs for formation of the emissive state and bleach recovery, respectively, suggest a branching ratio of 59 to 41%, which is consistent with the relative amplitudes from the components of the ground state bleach recovery (Figure 2).

The femtosecond transient absorption time range (3 ns) is insufficient to measure the lifetime of the long-lived ( $\sim 10 \mu\text{s}$ ) dark state giving rise to blinking on the single molecule level; therefore, nanoseconds–microseconds transient absorption was also performed. Interestingly, we previously reported that the  $\sim 10 \mu\text{s}$  lived Ag710 dark state not only gives rise to blinking, but also can be optically excited to further increase emission rates.<sup>15</sup> Nanosecond transient spectra indicate the formation of a long-lived charge-transfer state, presumably through a transition mediated by the initial fast charge transfer. The rise-time dynamics of this long-lived charge separated state (state 3) were instrument-response limited ( $\sim 7$  ns). Though the ground-state absorptions differ for each nanodot, transient absorption studies reveal strikingly similar spectra in the nanosecond (Figures 3A–C) to microsecond (Figure 4) time region. As with the femtoseconds transient data, the nanoseconds–microseconds transient absorption and bleach spectra were separated by subtracting a scaled version of the ground state absorption band for all of the species. The extracted transient absorption spectra show that there is indeed a broad peak across the visible and near-IR (Figure 3D) whose peak wavelength is common to all nanodots studied.

We measured the absorption cross section of this excited state absorption band by the singlet depletion method, given by the following relations<sup>31</sup>

$$\Delta OD_{\text{state0}} = -\epsilon_0[\text{state3}]l \quad (2)$$

$$\Delta OD_{\text{state3}} = \epsilon_3[\text{state3}]l \quad (3)$$

in which  $\epsilon$ 's are the molar extinction coefficients of the ground (state 0) and long-lived dark states (state 3),  $[\text{state 3}]$  is the concentration of the long-lived dark state, and  $l$  is the cell path length. It is assumed that all molecules excited into the first excited-state either return to the ground state or populate state 3 at  $t = 60$  ns. Additionally, an isosbestic point is seen in the decaying transient spectrum (Figure 5), suggesting that the excited-state population nearly quantitatively returns to the ground state. Because the ground-state and transient absorption spectra overlap, the extinction coefficient at the isosbestic point is identical for the two states ( $\epsilon_3(\lambda_c) = \epsilon_0(\lambda_c)$ ), in which  $\lambda_c$  is the isosbestic point. For the Ag660

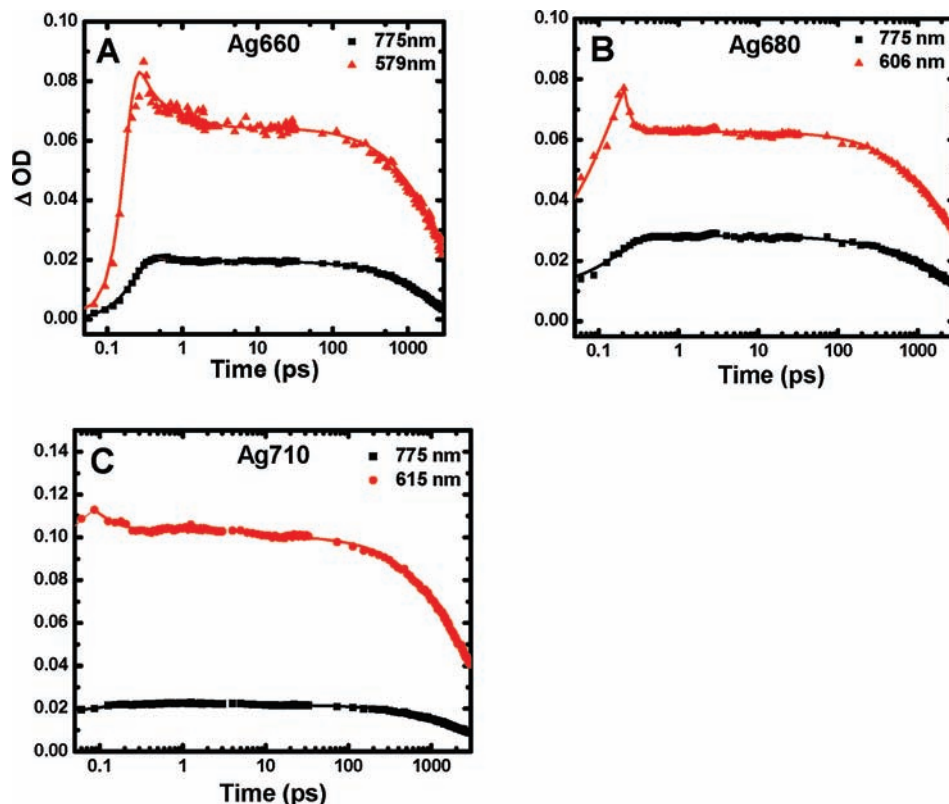


**Figure 2.** Femtosecond transient absorption kinetic traces. The wavelengths shown for each emitter reflect the transient absorption (black) and the ground-state depletion (red). The depletion shown appears at negative  $\Delta\text{OD}$  but is plotted in its absolute value. It has been corrected for spectral overlap by subtracting out the contribution from the transient absorption, which is based on the kinetics at 775 nm calibrated to the expected value based on the peak curve fittings. The data was collected by exciting with a 100 fs Ti-sapphire laser at 1 kHz, then probing with a white-light continuum generated from the same laser. The excitation wavelength was tuned to the peak of the ground-state absorption for each emitter.

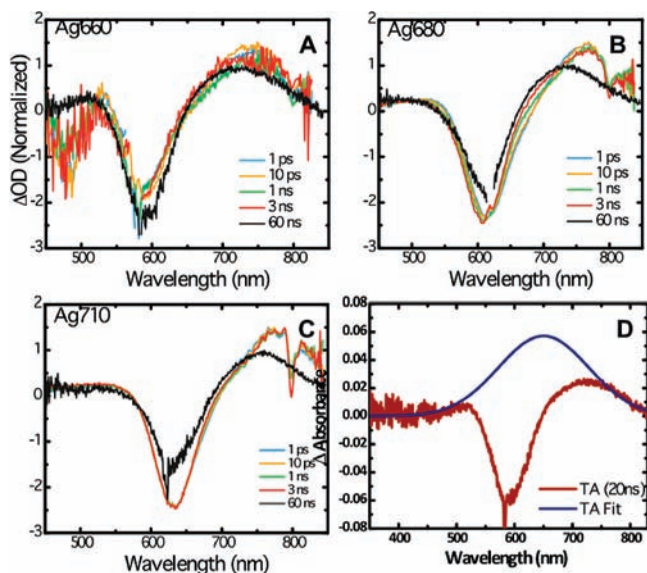


**Figure 3.** (A–C) Femtosecond and nanosecond transient absorption spectra (normalized) of a series of silver clusters, labeled by the maximum emission wavelength. All of the species were excited by 100 fs pulsed excitation, except for the long delay time curve, which was generated from excitation by a 7 ns pulsed laser. The dip in the spectrum around 800 nm is an instrumental artifact resulting from the white-light generation used as the probe. (D) The transient absorption and spectral fit of the Ag660 emitter, which was fitted to the 20 ns delay absorption curve, revealing a broad peak centered at 650 nm.

emitter, the isosbestic point occurs at 648 nm (Figure 5), where the ground-state extinction coefficient has the value  $1.2 \times 10^5 \text{ M}^{-1} \text{ cm}^{-1}$ ,<sup>32</sup> equal to the dark-state extinction coefficient at the same

**TABLE 1: Femtosecond Transient Absorption Kinetics**

	$\tau_{01}^{\text{GS}}$ (ps)	$\tau_{10}^{\text{CT}}$ (ps)	$\tau_{12}^{\text{CT}}$		$\tau_{20}^{\text{GS}}$ (ps)	$\tau_{20}^{\text{CT}}$ (ps)
			(ps) rise			
Ag660	$0.13 \pm 0.03$	$0.50 \pm 0.1$	$0.35 \pm 0.05$		$2140 \pm 78$	$2100 \pm 180$
Ag680	$0.14 \pm 0.05$	$0.38 \pm 0.1$	$0.21 \pm 0.04$		$1750 \pm 25$	$1860 \pm 100$
Ag710	$0.19 \pm 0.02$	$0.34 \pm 0.1$	$0.32 \pm 0.07$		$2240 \pm 69$	$2320 \pm 120$

wavelength. The peak dark-state extinction coefficient was then determined to be  $1.5 \times 10^5 \text{ M}^{-1} \text{ cm}^{-1}$  (absorption cross section of  $5.8 \times 10^{-16} \text{ cm}^2$ ) at 655 nm, based on the bleach correction of the transient absorption with values for all nanodots being listed in Table 2. The Ag660 transient decayed biexponentially with 10  $\mu\text{s}$  (35%) and 40  $\mu\text{s}$  (65%) time constants (Figure 6). Biexponential decays were observed in all the emitters (Table 2), suggesting that two states with indistinguishable transient spectra are populated. A stretched exponential model, however, could also faithfully fit the observed decay.

Formation of the microsecond lifetime dark state (state 3) renders the nanodot unable to fluoresce until the emissive manifold is repopulated. These dynamics are also manifested as fluorescence intermittency on the single molecule scale.<sup>16</sup> Correlations of individual photon time traces can be used to elucidate the dark state formation rate, decay rate, and quantum yield. Fluorescence correlation spectroscopy (FCS) was used to record photon time traces and generate single molecule dynamic information. The off-times, which correspond to the long-lived dark state decay time ( $\tau_{\text{dark}}$ ), were extracted using exponential fits of the autocorrelation decays (autocorrelation time,  $\tau_{\text{ac}}$ ) and the steady-state dark-state (state 3) population fraction ( $F_{\text{DS}}$ , obtained from the correlation amplitude), with<sup>33</sup>

$$k_{30} = \frac{1}{\tau_{AC}}(1 - F_{DS}) \quad (4)$$

$$k'_{30} = k_{30} + \sigma_3 I_{ex} \quad (5)$$

in which  $k'_{30}$  is the observed decay rate of the long-lived dark state with contributions from both the natural decay rate  $k_{30}$  and the excited-state absorption repopulating the emissive transition manifold. Time traces at several excitation intensities were measured, and the autocorrelation curves were fit to extract the time constants (Figure 7).<sup>34</sup> The natural decay rate was calculated by extrapolation of the linear fit to zero intensity. The slope of the fit was used to extract the excited-state absorption cross sections. Both the decay rate and absorption cross section were compared with the values obtained using solution transient absorption data. The transient absorption decay rate is taken as the natural decay rate, as no observable pump energy dependence was found. The single molecule intensity correlation analysis convolutes all off-times and models them as a single component, giving only one time constant.

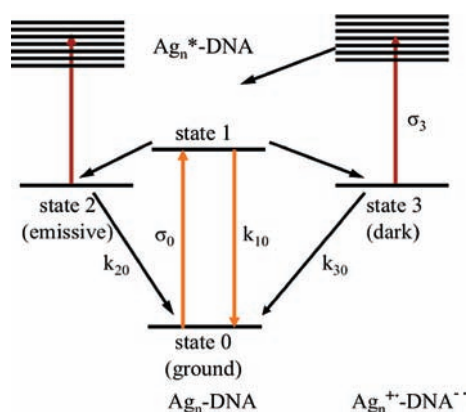


**Figure 4.** Energy diagram of the photoinduced charge transfer scheme. The Ag<sub>n</sub><sup>+</sup>-DNA complex is initially excited to the excited state of the silver cluster from which either a decay to the radiative state or the transition to the charge-transfer (CT) state occurs. The CT state can then either relax nonradiatively back to the ground state or transition into a longer-lived CT state from which photoassisted reverse charge transfer can occur.

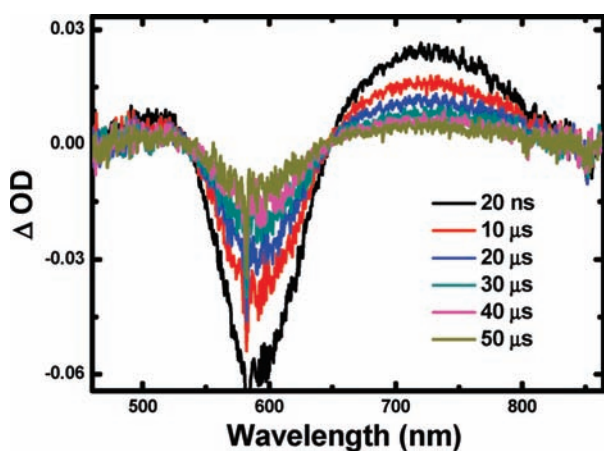


**Figure 5.** Nanosecond transient absorption spectra of the Ag660 nanodot at varying time delays. The curves clearly show an isosbestic point with delay at 648 nm, suggesting that depletion of the ground state at 595 nm leads to population of a state responsible for the positive change in absorbance at longer wavelengths. The nanodot was pumped with a several nanoseconds pulse at 590 nm.

Additionally, the faster decay components up to the nanosecond scale are beyond the experimental time window, and only the longer-lived off-time is experimentally observable with FCS. A weighted average of the biexponential decay components of nanosecond transient absorption was used to compare decay constants with those measured by FCS. For the Ag660 species, the natural decay time constant from FCS (31 μs) was found to be slightly larger than that obtained from transient absorption (20 μs). As shown in Table 2, similar agreement was observed for the 680 and 710 nm emitters.

#### IV. Discussion

The similarity of blinking time scales and transient absorption spectra suggests a mechanism common to all of the nanodots. Although clusters likely differ in size and geometry, the ssDNA scaffold is a consistent feature of all nanodots studied. Further, although drastic variations in both formation efficiency and stabilization as a function of pH have been reported, the endocyclic amine group of cytosine<sup>35</sup> remains the most likely binding site for Ag clusters, suggesting a silver-cytosine electronic interaction that facilitates initial formation and stabilizes the cluster upon reduction. The presence of cytosine is indeed critical to cluster formation,<sup>7,16,32,36,37</sup> and all of the clusters discussed presently contain multiple cytosine bases in the encapsulating DNA scaffold sequence.<sup>7,29</sup> The similarities among differently absorbing nanodot species, coupled with the strong, broad near-IR transient absorption reminiscent of the hydrated electron absorption,<sup>11,38</sup> suggest that a common, charge-transfer mechanism possibly gives rise to the photoinduced dark states in the nanodot emitters. Both gas phase and condensed-phase studies of anionic pyrimidines show that there is an experimentally observed and theoretically predicted absorption centered between 650 and 800 nm in aqueous solutions.<sup>39–41</sup> Transient absorption measurements of pyrene-deoxynucleotide coupled systems also show a broad, red absorption band with slow recombination rates.<sup>26</sup> In both cases, the peak was identified as anionic nucleotide absorption decaying via charge recombination. As the nanodot transient absorption persists in the presence of acetone,<sup>11,42</sup> and the transient signal rapidly and faithfully decays with repopulation of the emissive manifold upon irradiation, the DNA strand is the likely acceptor facilitating recombination, without the hydrated electron formation typically associated with unprotected Ag clusters.

The femtosecond transient absorption clearly indicates the presence of an initially formed excited state that rapidly bifurcates into creation (~350 fs rise) of a long-lived excited state that decays with the fluorescence lifetime and slightly slower (~500 fs) bleach recovery. The ratio of these decays reasonably models the observed partitioning into these two channels. Further, the action spectra,<sup>15</sup> FCS, and nanoseconds–microseconds transient absorption experiments all clearly show an even longer-lived transient (state 3, ~10 μs) with overlapping but slightly higher energy absorption compared to the emissive state 2. Further, the long-lived transient exhibits a fast rise time, suggesting that it does not arise from state 2, as the ~1% quantum yield of the trap state would indicate an easily observed rise time of ~300 ns, if arising from state 2. Consequently, we suggest that the initially formed state 1 with substantial charge separation rapidly separates into two channels: initial recombination to (1) mostly recover the ground state and (2) generate the fluorescent excited state 2, both within several hundred femtoseconds but with slightly different time constants. The much longer-lived state 3, suggestive of anionic cytosine,<sup>39</sup> must also be formed rapidly, and it is likely a trap state

TABLE 2: Excited-State Photophysical Properties

	$\lambda_{\text{abs}}$ (nm)	$\sigma^{\text{RCT}}$ ( $10^{-16}\text{cm}^2$ ) <sup>a</sup>	$\tau_1^{\text{CT}}$ ( $\mu\text{s}$ )	$\tau_2^{\text{CT}}$ ( $\mu\text{s}$ )	$\tau_{\text{wt}}^{\text{CT}}$ ( $\mu\text{s}$ ) <sup>b</sup>	$\tau^{\text{CT}}$ ( $\mu\text{s}$ ) <sup>c</sup>	$\phi_{\text{CT}}$ (TA) <sup>d</sup>	$\phi_{\text{CT}}$ (FCS) <sup>e</sup>
Ag660	595	5.8	10 (35%)	40 (65%)	19.5	31.1	0.746	$0.007 \pm 0.002$
Ag680	620	7.3	8.4 (84%)	20 (16%)	9.3	13.1	0.810	$0.008 \pm 0.002$
Ag710	633	4.2	4.7 (13%)	10 (87%)	8.7	16.3	0.86	$0.004 \pm 0.002$

<sup>a</sup> Absorption cross sections were measured by nanosecond transient absorption, described in ref 22. <sup>b</sup> The average decays from the transient absorption were calculated by taking the weighted inverse average of the two components  $1/\tau_{\text{wt}} = [A_1/(A_1 + A_2)](1/\tau_1) + [A_2/(A_1 + A_2)](1/\tau_2)$ . <sup>c</sup> The decay as measured by single-molecule correlation spectroscopy. The value was corrected for excited-state depopulation due to the excitation laser by extrapolating the intensity-dependent value to zero excitation intensity. <sup>d</sup> Determined by femtosecond transient absorption measurements. <sup>e</sup> Measured by single-molecule fluorescence correlation spectroscopy.

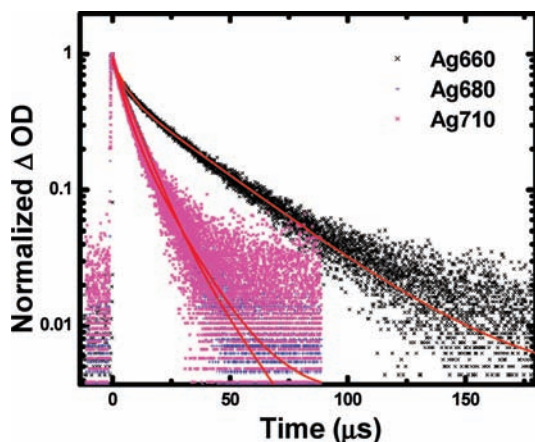


**Figure 6.** Transient absorption decay measurements. The decays were recorded at 770 nm using an oscilloscope-recorded photoreceiver response, whose instrument response time was 10 ns. Each decay was fitted biexponentially.

resulting from the initial charge separation. The model suggesting that the trap decays from the initial charge separated state is further supported by the solvent dependence of the Stokes shift discussed previously. The negative slope of the Stokes shift as a function of reaction field indicates that the dipole change in absorption is larger than the dipole change in emission, suggesting that a charge separated trap (state 3) likely evolves from state 1, instead of from the longer-lived, fluorescent state 2. If instead dark state population arose from the emissive level, the measured dark state quantum yield ( $\sim 1\%$ , see below for discussion) does not change, but only the rate constant for forming the dark state must be reduced, as it is then competing with the decay of the excited emissive level ( $\sim 3$  ns).

Photoinduced charge transfer requires the photon energy absorbed to drive the electron transfer. The Rehm–Weller

equation can be used to calculate the driving force of photoinduced CT, given by<sup>30</sup>

$$\Delta G = E_{\text{D+D}} - E_{\text{A/A}^-} - E_{00} - E_{\text{C}} \quad (6)$$

in which  $E_{\text{D+D}}$  is the reduction potential of the donor,  $E_{\text{A/A}^-}$  is the reduction potential of the acceptor,  $E_{00}$  is the ground-state absorption energy, and the last term ( $E_{\text{C}}$ ) is the Coulombic attraction energy experienced by the ion pair after charge transfer. The standard reduction potential of oligocytosine ( $\text{C}_9$ ) has been reported to be  $-1.6$  V.<sup>43</sup> Henglein et al. has reported the standard reduction potentials of silver clusters as a function of size ( $n = 1, 2, 3, 5$ ).<sup>12</sup> Combining the half-cell values, the expected photon energies required to induce charge transfer fall within the range of the silver cluster excitation energies (2.0–2.4 eV). The Coulombic energy term, though not known, can only drive the reaction further. Therefore the driving force is estimated to be sufficiently high for photoinduced charge transfer to cytosine from clusters of 2 Ag atoms or larger. Though the specific assignments of cluster size and geometry to excitation/emission energy have not been made, it has been previously argued that the clusters have sizes of 2–8 atoms based on mass spectral evidence and the small hydrodynamic radii,<sup>6,44</sup> but sizes could range as high as even 20 atoms.<sup>8,45,46</sup> These latter sizes are likely to increase the hydrodynamic radius beyond the measured levels, however.

The calculated driving forces suggest that although the forward photoinduced driving forces are “normal” ( $\Delta G \leq 0.5$  eV), the reverse direction has a significantly larger driving force ( $\Delta G \sim 2$  eV) that would be well into the inverted region. The recombination rate would then be dependent on relative changes in nuclear coordinate, tunneling, and Franck–Condon (FC) overlaps. FC overlaps between anionic and neutral cytosine are likely poor with a significant geometry change, while coupling of low quantum number cationic cluster vibrations with what are likely to be continuum states above the ground-state Ag cluster dissociation

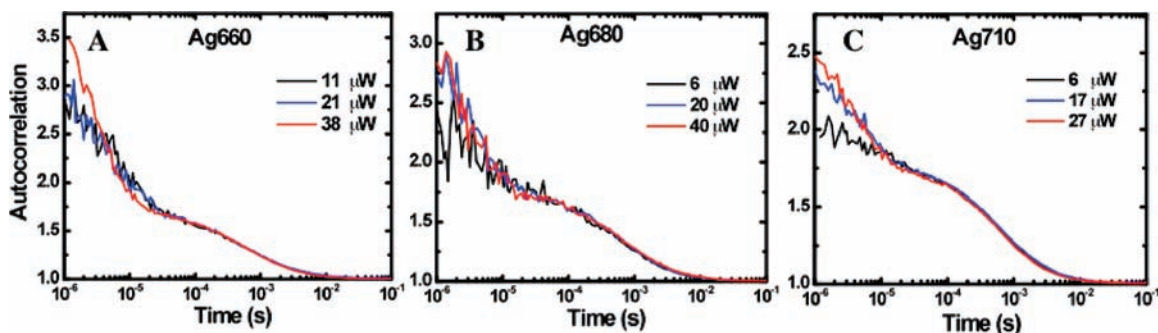


**Figure 7.** (A–C) Fluorescence correlation spectroscopy time trace autocorrelations for the three Ag nanodots. The species were excited (594, 633 nm HeNe) by a focused laser (60 $\times$  water objective, 1.2 NA) at the specified powers, and time traces were collected by an avalanche photodiode through a 50  $\mu\text{m}$  optical fiber. Two decay components were fitted, the longer time scale corresponding to diffusion through the laser focus, while the shorter time decay was attributed to the charge separated dark state.

threshold<sup>9</sup> may also be poor.<sup>47</sup> Coupled with the large driving force requiring very large reorganization energies, very slow recombination rates compared to the initial charge separation are expected.<sup>48–51</sup> Even without the Ag cluster and its poor vibrational overlap with the charge separated state, long-lived charge separated states have indeed been seen both in DNA and other molecular systems resulting from inverted region dynamics.<sup>52,53</sup>

Within the above assumed charge transfer model, the rate of charge transfer ( $k_{13}$ ) can be calculated using the single molecule autocorrelation times measured with FCS. The value is given by<sup>33</sup>

$$k_{13} = \frac{F_{\text{DS}}}{\tau_{\text{AC}}} \left( 1 + \frac{k'_{30}}{k_{01}} \right) \quad (7)$$

in which  $k_{01}$  is the excitation rate. The nonradiative decay rate ( $k_{10}$ ) was used in place of the normally used radiative rate ( $k_{20}$ ), because according to the proposed model, population of the long-lived CT state competes with nonradiative decay (1-0) and population of the emissive state (1-2) rather than with fluorescence (2-0). Within this model, the charge transfer rate constant for the Ag660 emitter is  $3.36 \times 10^{10} \text{ s}^{-1}$  based on an excitation rate of  $2.21 \times 10^7 \text{ s}^{-1}$ . The quantum yield of CT is then calculated based on the decay competition by  $\phi_3 = k_{13}/(k_{10} + k_{12} + k_{13})$ . The total calculated quantum yield is then  $\sim 0.7\%$ . For all three near-IR emitters, quantum yields ranging between 0.4 to 0.8% were calculated. This quantum yield value reflects the overall probability of populating the microsecond-lived trap states from initial excitation, without passing through the emissive state 2.

#### IV. Conclusion

The microsecond blinking dynamics observed on the single molecule level for silver nanodots has been shown to correspond to a spectrally observable, transient dark state. This state is proposed to be the result of photoexcited charge transfer to the encapsulating ss-DNA. Although initial charge separation is nearly instantaneous, forward charge transfer and trapping also occurs at fast rates ( $\sim 10^{11} \text{ s}^{-1}$ ) while recombination can occur very slowly ( $\sim 10^4 \text{ s}^{-1}$ ). The photoaccessibility and large cross sections of the CT state enable significant repopulation of the emissive manifold upon excitation by relatively low ( $\sim 5 \text{ kW/cm}^2$ ) secondary laser excitation intensities. This allows the already bright and photostable nanodot emitters to be used as optically modulatable probes for improved sensitivity.<sup>15</sup> The DNA provides a stable, photoaccessible charge accepting site, enabling photoexcited back-electron transfer. The charge transfer mechanism proposed here is ubiquitous among all fully reduced DNA-encapsulating silver nanodots examined.

**Acknowledgment.** This material is based upon work supported in part by NIH R01-GM068732 (R.M.D.) and NIH R. Kirchstein NRSA F31EB008324 (C.I.R.), the National Science Foundation NIRT Program (DMR 0454533) (J.W.P.) and U.S. Army Research Office (Grant 50372-CH-MUR) (J.W.P.). T.V. acknowledges support from an FWO fellowship. S.A.P. would like also to thank M. Malicki for many helpful discussions.

#### References and Notes

- (1) Widengren, J.; Schwille, P. *J. Phys. Chem. A* **2000**, *104*, 6416.
- (2) Yip, W. T.; Hu, D. H.; Yu, J.; Vanden Bout, D. A.; Barbara, P. F. *J. Phys. Chem. A* **1998**, *102*, 7564.
- (3) Verberk, R.; van Oijen, A. M.; Orrit, M. *Phys. Rev. B* **2002**, *66*, 4.
- (4) Kreibig, U.; Vollmer, M. *Optical Properties of Metal Clusters*; Springer: Berlin, 1995; Vol. 25.
- (5) Johnston, R. L. *Atomic and Molecular Clusters*; Taylor & Francis: London, 2002.

- (6) Petty, J. T.; Zheng, J.; Hud, N. V.; Dickson, R. M. *J. Am. Chem. Soc.* **2004**, *126*, 5207.
- (7) Richards, C. I.; Choi, S.; Hsiang, J. C.; Antoku, Y.; Vosch, T.; Bongiorno, A.; Tzeng, Y. L.; Dickson, R. M. *J. Am. Chem. Soc.* **2008**, *130*, 5038.
- (8) Zheng, J.; Nicovich, P. R.; Dickson, R. M. *Annu. Rev. Phys. Chem.* **2007**, *58*, 409.
- (9) Konig, L.; Rabin, I.; Schulze, W.; Ertl, G. *Science* **1996**, *274*, 1353.
- (10) de Heer, W. A. *Rev. Mod. Phys.* **1993**, *65*, 611.
- (11) Linnert, T.; Mulvaney, P.; Henglein, A.; Weller, H. *J. Am. Chem. Soc.* **1990**, *112*, 4657.
- (12) Henglein, A.; Mulvaney, P.; Linnert, T. *Faraday Discuss.* **1991**, *31*.
- (13) Yu, J.; Choi, S.; Dickson, R. M. *Angew. Chem., Int. Ed.* **2009**, *48*, 318.
- (14) Yu, J.; Choi, S.; Richards, C. I.; Antoku, Y.; Dickson, R. M. *Photochem. Photobiol.* **2008**, *84*, 1435.
- (15) Richards, C. I.; Hsiang, J.-C.; Senapati, D.; Patel, S.; Yu, J.; Vosch, T.; Dickson, R. M. *J. Am. Chem. Soc.* **2009**, *131*, 4619.
- (16) Vosch, T.; Antoku, Y.; Hsiang, J.-C.; Richards, C. I.; Gonzalez, J. I.; Dickson, R. M. *Proc. Natl. Acad. Sci. U.S.A.* **2007**, *104*, 12616.
- (17) Heilemann, M.; Margeat, E.; Kasper, R.; Sauer, M.; Tinnefeld, P. *J. Am. Chem. Soc.* **2005**, *127*, 3801.
- (18) Kuno, M.; Fromm, D. P.; Hamann, H. F.; Gallagher, A.; Nesbitt, D. J. *J. Chem. Phys.* **2000**, *112*, 3117.
- (19) Bates, M.; Blosser, T. R.; Zhuang, X. *Phys. Rev. Lett.* **2005**, *94*, art. no. 108101.
- (20) Mao, S.; Benninger, R.; Yan, Y.; Petchprayoon, C.; Jackson, D.; Easley, C.; Piston, D.; Marriott, G. *Biophys. J.* **2008**, *94*, 4515.
- (21) Marriott, G.; Mao, S.; Sakata, T.; Ran, J.; Jackson, D. *Proc. Natl. Acad. Sci. U.S.A.* **2008**, *105*, 17789.
- (22) Hilpert, K.; Gingerich, K. A. *Ber. Bunsen-Ges. Phys. Chem.* **1980**, *84*, 739.
- (23) Shi, Y.; Spasov, V.; Ervin, K. J. *Chem. Phys.* **1999**, *111*, 938.
- (24) Ershov, B. G.; Janata, E.; Henglein, A. *J. Phys. Chem.* **1993**, *97*, 339.
- (25) Henglein, A. *Chem. Phys. Lett.* **1989**, *154*, 473.
- (26) Trifonov, A.; Buchvarov, I.; Wagenknecht, H. A.; Fiebig, T. *Chem. Phys. Lett.* **2005**, *409*, 277.
- (27) Huber, R.; Fiebig, T.; Wagenknecht, H. A. *Chem. Commun.* **2003**, 1878.
- (28) Raytchev, M.; Mayer, E.; Amann, N.; Wagenknecht, H. A.; Fiebig, T. *ChemPhysChem* **2004**, *5*, 706.
- (29) Patel, S. A.; Richards, C. I.; Hsiang, J. C.; Dickson, R. M. *J. Am. Chem. Soc.* **2008**, *130*, 11602.
- (30) Lakowicz, J. R. *Principles of Fluorescence Spectroscopy*, 3rd ed.; Springer, New York, 2006.
- (31) Carmichael, I.; Hug, G. L. *J. Phys. Chem. Ref. Data* **1986**, *15*, 1.
- (32) Antoku, Y. DNA-encapsulated Ag nanocluster fluorescence. Ph.D. Thesis, Georgia Institute of Technology, 2007.
- (33) Ringemann, C.; Schonle, A.; Giske, A.; von Middendorff, C.; Hell, S. W.; Eggeling, C. *ChemPhysChem* **2008**, *9*, 612.
- (34) Widengren, J.; Mets, U.; Rigler, R. *J. Phys. Chem.* **1995**, *99*, 13368.
- (35) Ritchie, C. M.; Johnsen, K. R.; Kiser, J. R.; Antoku, Y.; Dickson, R. M.; Petty, J. T. *J. Phys. Chem. C* **2007**, *111*, 175.
- (36) Gwinn, E. G.; O'Neill, P.; Guerrero, A. J.; Bouwmeester, D.; Fyngenson, D. K. *Adv. Mater.* **2008**, *20*, 279.
- (37) Marzilli, L. G.; Kistenmacher, T. J.; Rossi, M. *J. Am. Chem. Soc.* **1977**, *99*, 2797.
- (38) Tauber, M. J.; Mathies, R. A. *J. Phys. Chem. A* **2001**, *105*, 10952.
- (39) Schiedt, J.; Weinkauff, R.; Neumark, D. M.; Schlag, E. W. *Chem. Phys.* **1998**, *239*, 511.
- (40) Denifl, S.; Ptasinaka, S.; Cingel, M.; Matejcek, S.; Scheier, P.; Mark, T. D. *Chem. Phys. Lett.* **2003**, *377*, 74.
- (41) Richardson, N. A.; Gu, J. D.; Wang, S. Y.; Xie, Y. M.; Schaefer, H. F. *J. Am. Chem. Soc.* **2004**, *126*, 4404.
- (42) Tauber, M. J.; Stuart, C. M.; Mathies, R. A. *J. Am. Chem. Soc.* **2004**, *126*, 3414.
- (43) Trnkova, L.; Jelen, F.; Postbieglova, I. *Electroanalysis* **2003**, *15*, 1529.
- (44) Zheng, J.; Dickson, R. M. *J. Am. Chem. Soc.* **2002**, *124*, 13982.
- (45) Link, S.; Beeby, A.; FitzGerald, S.; El-Sayed, M. A.; Schaaff, T. G.; Whetten, R. L. *J. Phys. Chem. B* **2002**, *106*, 3410.
- (46) O'Neill, P. R.; Velazquez, L. R.; Dunn, D. G.; Gwinn, E. G.; Fyngenson, D. K. *J. Phys. Chem. C* **2009**, *113*, 4229.
- (47) Freed, K. F.; Jortner, J. *J. Chem. Phys.* **1970**, *52*, 6272.
- (48) Chen, P. Y.; Duesing, R.; Graff, D. K.; Meyer, T. J. *J. Phys. Chem.* **1991**, *95*, 5850.
- (49) Ohkubo, K.; Kotani, H.; Shao, J. G.; Ou, Z. P.; Kadish, K. M.; Li, G. L.; Pandey, R. K.; Fujitsuka, M.; Ito, O.; Imahori, H.; Fukuzumi, S. *Angew. Chem., Int. Ed.* **2004**, *43*, 853.
- (50) Liang, N.; Miller, J. R.; Closs, G. L. *J. Am. Chem. Soc.* **1990**, *112*, 5353.
- (51) Suppan, P. *Top. Curr. Chem.* **1992**, *163*, 95.
- (52) Shafirovich, V.; Levin, P.; Kuzmin, V.; Thorgeirsson, T.; Kligler, D.; Geacintov, N. *J. Am. Chem. Soc.* **1994**, *116*, 63.
- (53) Zahavy, E.; Fox, M. A. *J. Phys. Chem. B* **1999**, *103*, 9321.